Okhotsk Sea and Polar Oceans Research

Volume 2 (2018)

Okhotsk Sea and Polar Oceans Research Association

Mombetsu City, Hokkaido, Japan

General Information for OSPOR

(August, 2017)

1. Aims and Scope

Okhotsk Sea and Polar Oceans Research (OSPOR) is published by the Okhotsk Sea and Polar Oceans Research Association (OSPORA).

Since 1986 the Okhotsk Sea and Cold Ocean Research Association (OSCORA) has held the International Symposium at Mombetsu, Hokkaido, in Japan every February and has released its proceedings over 30 years. In 2017 OSCORA changed to OSPORA, because the Symposium scope was broadened ~~to~~ include ~~to~~ the polar oceans (the Arctic and Antarctic Oceans), the Arctic passages, global warming, and environmental change in Polar Regions.

OSPORA started a reviewed papers system from the 2017 Symposium. The papers are refereed by multiple reviewers, published in the proceedings of the Symposium with a title of “Article”, and opened on the OSPOR web site.

2. Subjects covered by OSPOR

1) Environment of Okhotsk Sea
2) Meteorology and oceanography in polar regions
3) Cold region engineering
4) Arctic sea routes
5) Global warming and environment change
6) Remote sensing
7) Snow, ice and human life
8) Other topics about Okhotsk Sea and Polar Oceans

3. Editorial Policy of OSPOR

We intend to publish article papers, which should contain original scientific results and relevant subjects about Okhotsk Sea and Polar Oceans, not submitted for publication elsewhere.

4. Editorial Board

Period: August 2016 - August 2018

Editor-in-Chief : Hiromitsu Kitagawa (Ocean Policy Research Foundation)

Editors : Hajo Eicken (University of Alaska Fairbanks, USA) (2017-2018)
Hiroyuki Enomoto (National Research Institute of Polar Researches, Japan)
Yutaka Michida (University of Tokyo, Japan)
Humio Mitsudera (Hokkaido University, Japan)
Koji Shimada (Tokyo University of Marine Science and Technology, Japan)
Shuhei Takahashi (Okhotsk Sea Ice Museum of Hokkaido, Japan)
Hajime Yamaguchi (University of Tokyo, Japan)

5. OSPOR website

Temporal website: http://www.o-tower.co.jp/okhsympo/top-index.html
E-mail: momsys@o-tower.co.jp

Cover photo: Sea ice at Mombetsu, Japan (photo by Shuhei Takahashi, 2003)
Back cover photo: Crab Scissors Monument at Mombetsu, Japan

Okhotsk Sea and Polar Oceans Research, Volume 2 (2018)
Published by the Okhotsk Sea and Polar Oceans Research Association (OSPORA),
Mombetsu City, Hokkaido, Japan

Okhotsk Sea and Polar Oceans Research (OSPOR)

Contents

Volume 2 (2018)

Okhotsk Sea and Polar Oceans Research 2 (2018) 1-6
© Okhotsk Sea and Polar Oceans Research Association
https://doi.org/10.57287/ospor.2.1

Article

An algorithm for estimating sea-ice type from AMSR-E data in the Beaufort Sea

Yasuhiro TANAKA[1], Kazutaka TATEYAMA[1] and Seita HOSHINO[2]

[1] *School of Engineering, Kitami Institute of Technology, Kitami, Hokkaido, Japan*
[2] *Graduate School of Engineering, Kitami Institute of Technology, Kitami, Hokkaido, Japan*

(Received September 20, 2017; Revised manuscript accepted November 29, 2017)

Abstract

This paper evaluates the validity of an algorithm for estimating sea-ice type from the Advanced Microwave Scanning Radiometer – Earth observing system data (AMSR-E ice type). We compared sea-ice age data on National Snow and Ice Data Center and AMSR-E ice type. The results show an agreement rate > 80% over October–April. This suggests that the algorithm for AMSR-E ice type is valid for distinguishing between first-year ice and multiyear ice during October–April, although the algorithm is affected by major factors such as snow depth and air temperature.

Key words: sea ice, ice type, Arctic Ocean, passive microwave, AMSR-E

1. INTRODUCTION

Sea ice is an essential component of the climate system. The Arctic sea-ice extent in September has accelerated from a rate of ice loss of 36,000 km^2 per year over 1979–1996 to 130,000 km^2 per year over 1997–2014 (Serreze and Stroeve, 2015). Additionally, winter ice volume retrieved using Ice, Cloud, and land Elevation Satellite (ICESat) and multiyear ice (MYI) extent retrieved using the Special Sensor Microwave Imager (SSM/I) decreased 21% in the 6 years over 2003–2008 and 15.6% per year over 1979–2010 (Kwok *et al*., 2009; Comiso, 2012). This means that Arctic ice thickness has declined.

Heat flux between the atmosphere and ocean for thinner ice was 2.3 times greater than that for thicker ice (Maykut *et al*., 1982). This result is similar to heat flux estimates based on Surface Heat Budget of the Arctic Ocean observations (Lindsay *et al*., 2003). Thus, the distributions of ice type and thickness are important factors for understanding heat flux through sea ice.

Studies have estimated ice thickness distributions by field measurements, submarines, satellites observation such as Microwave Imaging Radiometer with Aperture Synthesis, and ice motion modeling (e.g., Melling and Riedel, 1995; Fowler *et al*., 2004; Rothrock *et al*. 2008; Laxon *et al*., 2013). However, these observations are limited in spatial and temporal coverage.

Satellite passive microwave sensors are not affected by cloud cover and can be used to observe the entire Arctic during night and day. Iwamoto *et al*. (2014) developed a new algorithm for estimating thin ice thickness in the Arctic Ocean using Advanced Microwave Scanning Radiometer-Earth observing system (AMSR-E) data. However, it is difficult to estimate ice thickness in the Arctic Ocean with MYI. Moreover, Krishfield *et al*. (2014) proposed an algorithm for estimating ice type (and thickness) using AMSR-E data (AMSR-E ice type) for the Beaufort Sea. However, the algorithm for estimating AMSR-E ice type (AMSR-E ice-type algorithm) has yet to be evaluated.

We evaluated an AMSR-E ice-type algorithm that distinguishes between first-year ice (FYI) and MYI. MYI was second-year or older ice in our study. An examination of ice thickness results is underway in a separate paper.

2. DATA

Table 1 summarizes specifications of data products used in the present study. Daily mean brightness temperature (T_B) in the AMSR-E/Aqua Daily L3 product are provided by the National Snow and Ice Data Center (NSIDC). The 6.9 GHz channel data with both vertical (V) and horizontal (H) polarization, and 18.7, 23.8, and 36.5 GHz (V) channel data were used to estimate AMSR-E ice type and melt pond fraction (MPF).

Table 1. Specifications of data products

Data products	Parameters	Gridding interval	Temporal Coverage	Temporal resolution
AMSR-E/Aqua Daily L3	T_B	25 km x 25 km	Jun. 2002 to Oct. 2011.	Daily
MEaSUREs Arctic Sea Ice Characterization	Sea Ice Age	25 km x 25 km		
Global Sea Ice Concentration Climate Data Record v2.0	Sea Ice concentration	25 km x 25 km		
CFSR	Air temperature Snow depth	0.5° x 0.5°	Jun. 2002 to Dec. 2010	6 hourly
CFSv2			April. 2011 to Oct. 2011	

Sea-ice age in the NASA Making Earth System Data Records for Use in Research Environments Arctic Sea Ice characterization provided by NSIDC (NSIDC ice age) were used to compare AMSR-E ice type because projection of the two data sets is the same. The ice age output the oldest ice age values on each grid cell and between FYI and 10th-year ice, based on satellite remote sensing-based sea-ice motion data. This means that ice age was omitted the passages over the Canadian Arctic Archipelago. This remote sensing-based age is similar to buoy-derived age produced by Rigor and Wallace (2004) as shown in NSIDC.

Sea-ice concentration data in Global Sea Ice Concentration Climate Data Record (version 2.0) are available at the EUMETSAT Ocean and Sea Ice Satellite Application Facility (OSISAF), and include the product user manual (Sørensen *et al*., 2017) and validation report (Kreiner *et al*., 2017). The biases of the sea-ice concentration data in summer and other season were −5% and −1–−2%, respectively, compared to National Ice Center sea-ice charts. These data were retrieved from the European Space Agency Climate Change Initiative Sea Ice (phase 2) Low Frequency channels algorithm, which improved on the OSISAF “hybrid” algorithm (itself a combination of Bootstrap Freq-Mode and Bristol algorithms) (Tonboe *et al*., 2016).

The Climate Forecast System (CFS) Reanalysis and CFS Version 2 (CFSv2) data for 2-m air temperature and snow depth are produced and provided by the National Centers for Environmental Prediction (NCEP). These data were used to examine the effect of depth and air temperature on the AMSR-E ice-type algorithm. A NSIDC grid cell was taken from the nearest CFS grid cell. The snow depth in CFSs had a positive bias during winter (10–20 cm) and spring (5–25 cm), a negative bias during summer (−25–0 cm) and autumn (−5–10 cm), compared to the buoy-derived snow depth (Sato and Inoue, 2017).

3. AMSR-E ICE TYPE ALGORITHM

The AMSR-E ice-type algorithm for the Beaufort Sea (including background) is explained in detail in Krishfield *et al*. (2014) and is outlined here. Hereafter, V-polarization at frequency 18.7 GHz is expressed as T_{B18V}, and this convention is also used for the other channels. Cavalieri *et al*. (1984) reported that the gradient ratio (*GR*) between T_{B19V} and T_{B37V} in SSM/I data ($GR_{\mathrm{19V–37V}}$) is valid for distinguishing between FYI and MYI in the NASA team standard ice algorithm for the Arctic Ocean. This is because MYI has much lower salinity and less moisture (Ulaby *et al*., 1982).

Krishfield *et al*. (2014) defined the *GR* between T_{B18V} and T_{B36V} in AMSR-E data ($GR_{\mathrm{18V–36V}}$), which was compared with shipborne electromagnetic induction device thickness during late summer. $GR_{\mathrm{18V–36V}}$ is sensitive to change in ice thickness in MYI areas. This suggests that $GR_{\mathrm{18V–36V}}$ varies with ice temperature at penetration depths for 18.7 and 36.5 GHz channels, as well as snow depth over sea ice. $GR_{\mathrm{18V–36V}}$ accuracy was also examined by comparison with daily-average ice draft data from the upward looking sonar (ULS draft) mounted on the Beaufort Gyre observing system mooring. Thickness derived from $GR_{\mathrm{18V–36V}}$ is in agreement with the ULS draft in September. However, there is no agreement for other months. Therefore, *GR* was improved by using T_{B06V} and T_{B36V}, because the difference between 6 and 36 GHz is the largest, and so it is the most sensitive to the ULS draft. *GR* between T_{B06V} and T_{B36V} ($GR_{\mathrm{06V–36V}}$) are defined by the following equation.

$$GR_{06V-36V} = \frac{T_{B06V} - T_{B36V}}{T_{B06V} + T_{B36V}} \tag{1}$$

Using this definition of $GR_{\mathrm{06V–36V}}$, the range of $GR_{\mathrm{06V–36V}} \geq -0.025$ was considered FYI, and $GR_{\mathrm{06V–36V}} < -0.025$ was considered MYI.

4. RESULTS

To evaluate the validity of the AMSR-E ice-type algorithm, we compared NSIDC ice age and AMSR-E ice type and examined their agreement rate. For example, if NSIDC ice age indicated MYI, then the algorithm was correct when AMSR-E ice type indicated MYI. T_{B06V} and T_{B36V} for $GR_{\mathrm{06V–36V}}$ was affected by melt ponds during summer (May–August) (Tanaka *et al*., 2016). If the MPF (Eq. 2) was > 20%, grid cells were not included in the analysis.

$$MPF = 15.2 - 158.9\left(\frac{T_{B06H} - T_{B89V}}{T_{B06H} + T_{B89V}}\right) \tag{2}$$

Figure 1 shows seasonal change of mean agreement rate between NSIDC ice age and AMSR-E ice type. The maximum rate was 98% at the end of September. The rate decreased to 86% in December and was nearly constant from January to April. Subsequently, the rate in May decreased to 60%, and standard deviation of the rate also increased. Moreover, the number of grid cells declined during summer because cells with MPF > 15% were not included.

Figure 2 shows examples of the distributions of both NSIDC ice age and AMSR-E ice type. These distributions on 1 January and 1 April were similar. Agreement rates were respectively 91% and 90% on those dates. Although the rate was 88% on 1 September, it is difficult to understand the distribution of AMSR-E ice type across the entire Arctic Ocean. Additionally, FYI grid cells were situated between MYI grid cells in the distribution of NSIDC ice age (Figs. 2a, 2c, and 2e). This characteristic was not found in the distribution of AMSR-E ice type (Figs. 2b, 2d, and 2f).

Figure 3 shows seasonal change of mean $GR_{\mathrm{06V\text{-}36V}}$, air temperature, and snow depth. During the high agreement rate (October–April), the difference between mean $GR_{06V\text{-}36V}$ of FYI and MYI was 0.045. However, standard deviations of the rate for FYI and MYI were 0.035 and 0.03, respectively. This means that the change of $GR_{06V\text{-}36V}$ varied by year. The change of snow depth and air temperature behaved similarly.

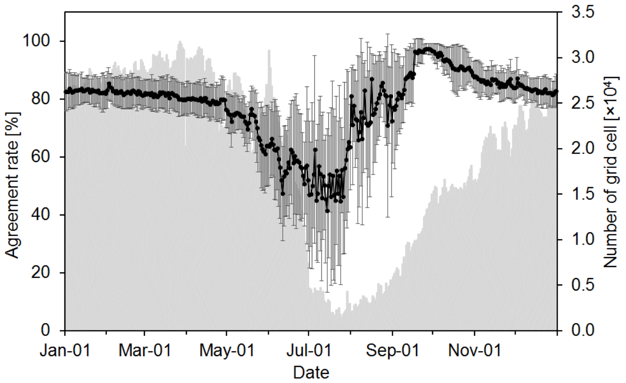

Fig. 1 Seasonal change of mean agreement rate between NSIDC ice age and AMSR-E ice type over the Beaufort Sea during 2002–2011, with standard deviations (vertical lines). Gray bars show number of grid cells.

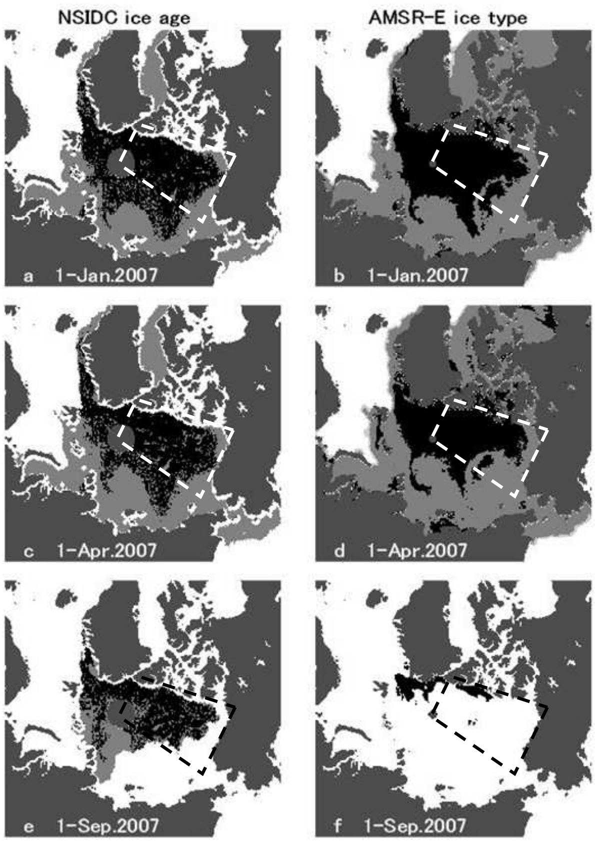

Fig. 2 Examples of NSIDC ice age (left panels) and AMSR-E ice type (right panels) distributions for January, April, and September 2007. Black, light gray, dark gray, and white are multiyear ice, first-year ice, land, and missing grid cells, respectively. A missing grid cell means > 20% melt pond fraction or open water (< 20% sea-ice concentration). Analysis area in this study exists inside the trapezoid.

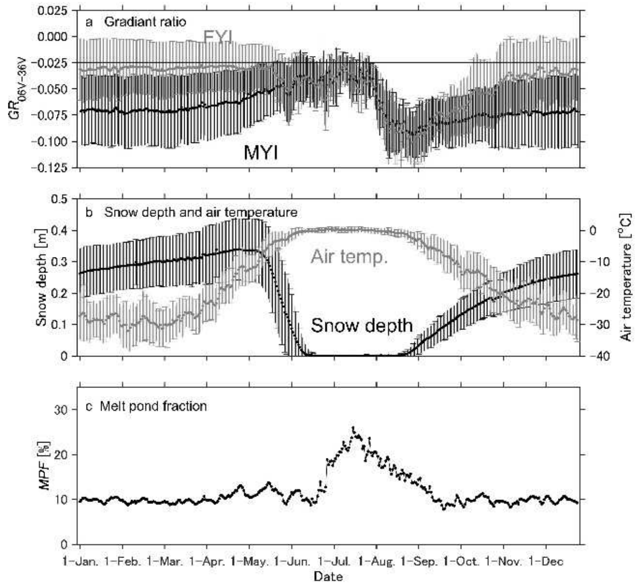

Fig. 3 Seasonal change of mean (a) $GR_{06V\text{-}36V}$ from calculated AMSR-E data, (b) air temperature and snow depth from CFSs with standard deviations (vertical lines), and (c) melt pond fraction from calculated AMSR-E data over the period 2002–2011 in the Beaufort Sea. Multiyear ice (MYI) and first-year ice (FYI) in panel (a) are from NSIDC ice age.

5. DISCUSSION

The agreement rate between NSIDC ice age and AMSR-E ice type is > 80 % for October to April. This demonstrates that the AMSR-E ice-type algorithm is valid for distinguishing FYI from MYI.

The agreement rate for 1 September is higher than that in other months. However, estimated areas of AMSR-E ice type (especially minimum sea-ice extent in September 2007 over the years 2002–2011) were limited by the effect of MPF (Fig. 2f). This indicates an unacceptable agreement rate in summer and September.

We now address the causes of the disagreement between NSIDC ice age and AMSR-E ice type. Eicken *et al*. (2002) and Perovich *et al*. (2009) reported that the salinity of thicker FYI (> 70 cm) is similar to that of MYI. Additionally, T_{B36V} for $GR_{06V–36V}$ was sensitive to the difference between FYI and MYI salinities. We believe that the AMSR-E ice-type algorithm regards thicker FYI as MYI.

The AMSR-E ice-type algorithm determines the dominant ice type in a grid cell. In contrast, NSIDC ice age outputs the oldest ice age in a grid cell if that cell includes ice of different ages. This does not necessarily output the dominant NSIDC ice age in a grid cell. Therefore, a cause for the disagreement may be the difference of determination method for AMSR-E ice type and NSIDC ice age.

We considered the effect of $GR_{06V–36V}$ on snow depth and air temperature. Relationships between $GR_{06V–36V}$

and snow depth and air temperature were examined as shown in Table 2. T_{B36V} decreased with snow depth (Eppler *et al.*, 1992). The relationship between $GR_{06V-36V}$ and snow depth tends to be strong for FYI in December (r = −0.51) and MYI in October (r = −0.53). As an example, $GR_{06V-36V}$ decreases with the increasing snow depth in October (Fig. 4a). Then, the increase of snow depth is 0.1 m per month (Fig. 3b). This suggests that change of snow depth affects $GR_{06V-36V}$. However, the increase of snow depth (0.01 m per month) during January–April is less (Fig. 3b). The relationship between $GR_{06V-36V}$ and snow depth is also weak (Table 2). According to Sato and Inoue (2017), snow depth in CFS data has a positive bias during winter and spring, greater than that during autumn. Therefore, we believe that the biases affect the relationship between $GR_{06V-36V}$ and snow depth as shown in Table 2.

Table 2. Correlation coefficients (r) and p-values between $GR_{06V-36V}$, and snow depth and air temperature for first-year ice (FYI) and multiyear ice (MYI) in the Beaufort Sea.

	Snow depth				Air temperature			
	FYI		MYI		FYI		MYI	
Month	r	p	r	p	r	p	r	p
1	-0.04		0.30	< 0.001	0.02	0.45	-0.22	0.45
2	0.05		0.31		-0.21	0.45	-0.29	0.45
3	0.43		0.50	0.35	-0.08	0.22	-0.02	0.22
4	0.25	< 0.001	0.32		-0.49		0.05	
10	-0.32		**-0.53**	< 0.001	0.27	< 0.001	**0.67**	< 0.001
11	-0.38		0.11		**0.51**		**0.93**	
12	**-0.51**		0.18		-0.40		0.28	

T_{BS} is affected by the relationship between surface temperature and air temperature. The relationship between $GR_{06V-36V}$ and air temperature tended to be strong for FYI (r = 0.51) and MYI (r = 0.93) in November. As shown in Fig. 4b, $GR_{06V-36V}$ increased with air temperature. However, the relationship between $GR_{06V-36V}$ and air temperature was weak during December–April. This suggests that the increase of air temperature (3 °C per month) was less than that during October and December (7 °C per month). Thus, $GR_{06V-36V}$ is affected by snow depth and air temperature in addition to ice type.

$GR_{06V-36V}$ tended to increase in October and November (Fig. 5). Trends of MYI in October and November were 0.0031 and 0.017 per year, respectively. Moreover, the differences between $GR_{06V-36V}$ for FYI and MYI were greater than those in November. These results suggest that the threshold for estimating AMSR-E ice type changes monthly and yearly. The threshold may need further improvement if ice types are retrieved using AMSR2 data since 2012.

The aforementioned findings will serve as a basis for further understanding of essential effects on the AMSR-E ice-type algorithm. Kimura *et al*. (2013) advanced the possibility that the ice thickness distribution in spring is affected by the redistribution of ice floes in winter. This is important for potential improvement in prediction of the summer ice area in spring by investigating winter ice motion. Moreover, information of sea-ice type in spring is useful for a prediction model of melt pond expansion (Eicken *et al*., 2004). This is because melt ponds in summer differ in their range of expansion on FYI and MYI and are a major influence on the ice–albedo feedback mechanism (e.g., Flocco *et al*., 2007; Schröder *et al*., 2014). Thus, the AMSR-E ice-type algorithm will also be useful for these predictions.

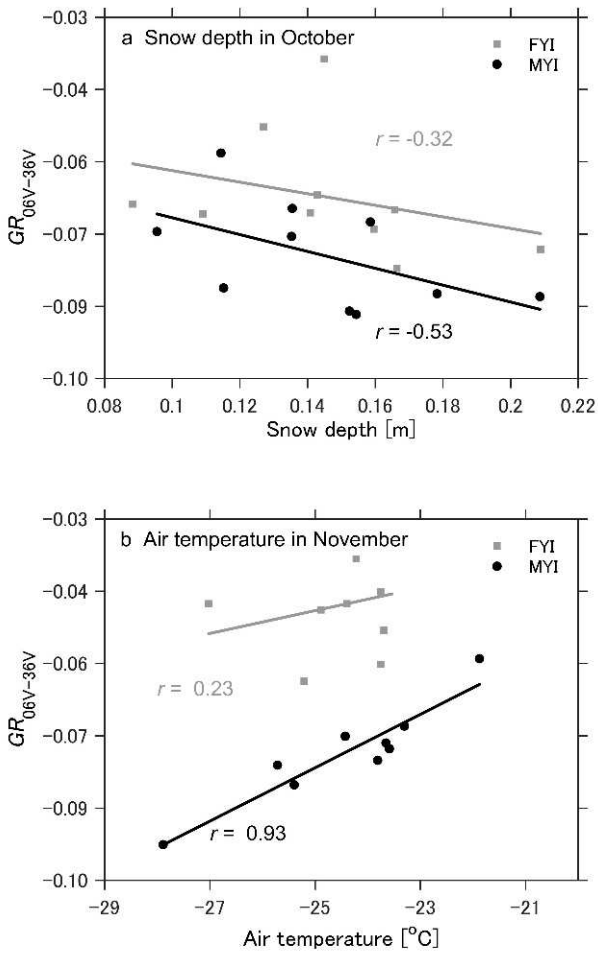

Fig. 4 Relationship between $GR_{06V-36V}$, and (a) snow depth in October and (b) air temperature in November over the period 2002–2011. r denotes the correlation coefficient for the Beaufort Sea. Solid lines in these panels show regression lines. These relationships are statistically significant at the 99.9% confidence level. FYI and MYI are first-year ice and multiyear ice, respectively.

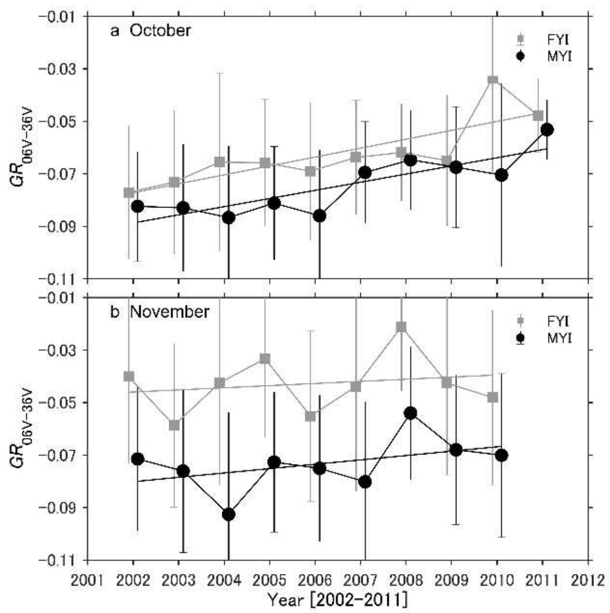

Fig. 5 Time series of $GR_{06V\text{-}36V}$ in (a) October and (b) November from 2002–2011 with standard deviations (vertical lines) in the Beaufort Sea. Solid lines in these panels show regression lines. FYI and MYI are first-year ice and multiyear ice, respectively.

6. CONCLUSIONS

We compared NSIDC ice age and AMSR-E ice type to evaluate the AMSR-E ice type algorithm. The study focused on area and period in the Beaufort Sea during October–April 2002–2011.

The agreement rate between NSIDC ice age and AMSR-E ice type exceeded 80% from October to April. This rate increased to 86% in December and was constant from January to April. The distributions of AMSR-E ice type in January and April 2007 were in agreement with those of NSIDC ice age. We believe that the major causes of disagreement were the following: (1) The algorithm regarded thicker FYI as MYI, and (2) snow depth and air temperature affected $GR_{06V–36V}$.

Although the AMSR-E ice-type algorithm was mainly influenced by the two factors above, the algorithm was valid for distinguishing FYI from MYI during October–April. Our findings will contribute to the improvement of algorithm accuracy. This will support accurate prediction of sea-ice cover, type and thickness, as well as the model of melt pond expansion.

ACKNOWLEDGMENTS

This study was supported by the Arctic Challenge for Sustainability (ArCS) Project. We appreciate Jun Inoue for helpful conversations during the course of this work. The products for brightness temperature and sea-ice age were obtained from the National Snow and Ice Data Center (NSIDC; http://nsidc.org/). The products for snow depth and air temperature were provided by the National Centers for Environmental Prediction Climate Forecast System Reanalysis (https://climatedataguide.ucar.). The global sea ice concentration climate data record 1978–2015 (version 2.0) was provided from the EUMETSAT Ocean and Sea Ice Satellite Application Facility (http://osisaf.met.no). We are grateful to Stefan Kern and Steinar Eastwood for their help with the products. We thank Steven Hunter, M.S, from Edanz Group (www.edanzediting.com/ac) for editing a draft of this manuscript.

REFERENCES

Cavalieri, D. J., P. Gloersen, and W. J. Campbell (1984): Determination of sea ice parameters with the NIMBUS 7 SMMR. *J. Geophys. Res.*, **89**: D4, 5355–5369.

Comiso, J. C. (2012): Large decadal decline of the Arctic multiyear ice cover. *J. Climate*, **25**(4), 1176–1193, doi: 10.1175/JCLI-D-11-00113.1.

Eppler, D. T. and 6 others (1992), Passive microwave signatures of sea ice, in Microwave Remote Sensing of Sea Ice. *Geophys. Monogr. Ser*., **68**, edited by F. D. Carsey, 47–71, AGU, Washington, D. C.

Eicken, H. and 3 others (2002): Tracer studies of pathways and rates of meltwater transport through Arctic summer sea ice. *J. Geophys. Res.*, **107**: C10, 8046, doi:10.1029/2000JC000583

Eicken, H. and 4 others (2004): Hydraulic controls of summer Arctic pack ice albedo. *J. Geophys. Res.*, **109**, C08007.

Flocco, D., and D. L. Feltham (2007): A continuum model of melt pond evolution on Arctic sea ice. *J. Geophys. Res.*, **112**: C08016.

Fowler, C., W. J. Emery, and J. Maslanik. (2004): Satellite-derived evolution of Arctic sea ice Age: October 1978 to March 2003. *Geoscience and Remote Sensing Letters, IEEE*, **1**(2), 71-74, doi: 10.1109/LGRS.2004.824741.

Iwamoto, K., K. I. Ohshima, and T. Tamura (2014), Improved mapping of sea ice production in the Arctic Ocean using AMSR-E thin ice thickness algorithm. *J. Geophys. Res. Oceans*, **119,** 3574–3594, doi:10.1002/ 2013JC009749.

Kimura, N. and 3 others (2013), Influence of winter sea ice motion on summer ice cover in the Arctic. *Polar Res.*, **32**, 2,0193, doi:10.3402/polar.v32i0.20.

Kreiner and 7 others (2017): Validation report for Global sea ice concentration reprocessing. EUMETSAT OSISAF Products OSI-450, Document version: 2.0.

Krishfield, R. A. and 6 others (2014): Deterioration of perennial sea ice in the Beaufort Gyre from 2003 to 2012 and its impact on the oceanic freshwater cycle. *J. Geophys. Res. Oceans*, **119**, 1271–1305, doi:10.1002/2013JC008999.

Kwok R., Cunningham G.F., Wensnahan M., Rigor I., Zwally H.J. & Yi D. 2009. Thinning and volume loss of the Arctic Ocean sea ice cover: 2003–2008. *J. Geophys. Res. Oceans*, **114**: C07005, doi: 10.1029/2009JC005312.

Lindsay, R.W. (2003): Changes in the modeled ice thickness distribution near the Surface Heat Budget of the Arctic Ocean (SHEBA) drifting ice camp. *J. Geophys. Res.*, **108**: C6, 3194.

Laxon, S. W. and 14 others (2013): CryoSat-2 estimates of Arctic sea ice thickness and volume. *Geophys. Res. Lett*., **40**, 732–737.

Maykut, G. A. (1982): Large-scale heat exchange and ice production in the central Arctic. *J. Geophys. Res.*, **87**: C10, 7971–7984.

Melling, H. and Riedel, D. A. (1995): The underside topo-graphy of sea ice over the continental shelf of the Beaufort

Sea in the winter of 1990. *J. Geophys. Res*., **100**: C7, 13,641–13,653.

Perovich, D. K. and 7 others (2009): Transpolar observations of the morphological properties of Arctic sea ice. *J. Geophys. Res.*, **114**, C00A04, doi:10.1029/2008JC004892.

Rigor, I. G., and J. M. Wallace (2004): Variations in the age of Arctic sea-ice and summer sea-ice extent. *Geophys. Res. Lett.*, **31**, L09401, doi:10.1029/2004GL019492.

Rothrock D.A., Percival D.B., and Wensnahan M. (2008): The decline in Arctic sea-ice thickness: separating the spatial, annual, and interannual variability in a quarter century of submarine data. *J. Geophys. Res. Oceans*, **113**: C05003, doi: 10.1029/2007JC004252.

Sato, K. and J. Inoue (2017): Comparison of Arctic sea ice thickness and snow depth estimates from CFSR with in situ observations. *Clim. Dyn.*, doi: 10.1007/s00382-017-3607-z.

Serreze, M. C. and J. Stroeve (2015): Arctic sea ice trends, variability and implications for seasonal ice forecasting. Philos. *Trans. Roy. Soc. London*, **373**, 20140159, doi:10.1098/rsta.2014. 0159.

Sørensen, A. M., Lavergne. T., and Eastwood S. (2017): Global Sea Ice Concentration Reprocessing. Product *User Manual, EUMETSAT OSISAF, Document version*: 1.0, Data set version: 2.0.

Schröder, D. and 3 others (2014): September Arctic sea-ice minimum predicted by spring melt-pond fraction. *Nature Climate Change*, **4**, 353–357.

Tanaka, Y., K. Tateyama, T. Kameda, and J. K. Hutchings (2016): Estimation of melt pond fraction over high-concentration Arctic sea ice using AMSR-E passive microwave data. *J. Geophys. Res. Oceans*, **121**, 7056–7072, doi:10.1002/2016JC011876.

Tonboe, R. T. and 7 others (2016): The EUMETSAT sea ice concentration climate data record. *The Cryosphere*, **10**, 2275-2290, doi:10.5194/tc-10-2275-2016.

Ulaby, F. T., R. K. Moore, and A. K. Fung (1982): Microwave Remote Sensing, Active and Passive, Vol. II - Radar Remote Sensing and Surface Scattering and Emission Theory, 609 pp., Artech House, Inc., Dedham, Massachusetts.

Summary in Japanese
和文要約

AMSR−E データによるボーフォート海の海氷の種類判別手法

田中康弘[1], 舘山一孝[1], 星野聖太[2]

[1]北見工業大学工学部, [2]北見工業大学大学院工学研究科

海氷は気候システムの重要な構成要素の一つである. 海氷の種類は, 海氷域における大気−海洋間の熱交換の影響を知るために重要である. 本研究では, 衛星マイクロ波放射計 AMSR-E データによる海氷の種類判別手法の有効性を評価した. この手法による海氷の種類と NSIDC による海氷年齢を比較した結果, 一致率は 10 月から 4 月の間で 80%を示した. これは秋から冬の間, AMSR-E による海氷の種類判別手法が一年氷と多年氷の判別に有効であると考えられる. また, その手法での一年氷と多年氷の判別閾値は, 積雪深や気温に影響されることがわかった. 今後は, 世界最高水準の AMSR2 データによる海氷の種類判別手法の開発を目指す.

Copyright ©2018 The Okhotsk Sea & Polar Oceans Research Association.　All rights reserved.

Okhotsk Sea and Polar Oceans Research 2 (2018) 7-12
© Okhotsk Sea and Polar Oceans Research Association
https://doi.org/10.57287/ospor.2.7

Article

Comparison of the Arctic tropospheric structures from the ERA-Interim reanalysis with in situ observations

Jun INOUE[1], Kazutoshi SATO[2] and Kazuhiro OSHIMA[3]

[1]*Natinoal Institute of Polar Research, Tachikawa, Japan*
[2]*Antarctic Climate & Ecosystems Cooperative Research Centre, Tasmania, Australia*
[3]*Japan Agency for Marine-Earth Science and Technology, Yokosuka, Japan*

(Received August 29, 2017; Revised manuscript accepted January 12, 2018)

Abstract

Using data sets of frequent radiosonde observations and surface meteorological observations obtained during an Arctic cruise in September 2014, the reproducibility of the ERA-Interim reanalysis product was evaluated with reference to the upper troposphere. Relative humidity in the ERA-Interim reanalysis was found overestimated with a positive bias of cloud cover in the upper troposphere, which was attributable partly to the parameterization of cloud formation. Relative humidity in the lower stratosphere was also higher than observed, suggesting that a small amount of moisture was transported from the troposphere to the stratosphere via mixing induced by radiative/evaporative cooling at the level of the excessive upper cloud. Ozone profiles, based on ozonesonde observations, revealed that a positive bias of ozone partial pressure below the tropopause in the ERA-Interim reanalysis could be attributed to downward transport of ozone from the lower stratosphere into the upper troposphere via entrainment of a high-ozone air mass. The positive bias of upper cloud in the ERA-Interim reanalysis also affected downward radiation at the surface for the case of absent boundary layer clouds.

Key words: Arctic, reanalysis, cloud, ozone, surface radiation

1. INTRODUCTION

Arctic cloud is one of the most important components of the Arctic climate system for determining surface heat budgets over both the sea ice and the open ocean. However, it is known that the reproducibility of Arctic cloud in climate models is inadequate and that its evaluation is difficult because of the lack of observations for validation purposes (e.g., surface boundary conditions, boundary layer profiles, and aerosol/condensation nuclei). Several special field campaigns and model intercomparison projects have been performed to try to overcome this difficulty and to develop parameterizations related to clouds (e.g., Curry *et al.*, 2000; Uttal *et al.*, 2002; Curry and Lynch, 2002). Cloud-top radiative cooling enhances the vertical mixing of heat, moisture, and momentum in the boundary layer (e.g., Nicholls and Leighton, 1986), but it is a very complicated process and it is hard to observe without aircraft. In addition, multiple layers of cloud in the Arctic, which consist of stable boundary layer clouds near the surface and mid-/upper-layer clouds associated with cyclones, make it difficult to understand the surface heat budget (e.g., Inoue *et al.*, 2005; 2006).

The ERA-Interim reanalysis product (Dee *et al.*, 2002) is known as one of the best reanalysis products for Arctic research (Inoue *et al.*, 2011; Lyndsay *et al.*, 2014), although cloud cover is also reproduced well in other reanalysis products (Liu and Key, 2016). Although lower boundary layer clouds have been investigated and compared with in situ observations

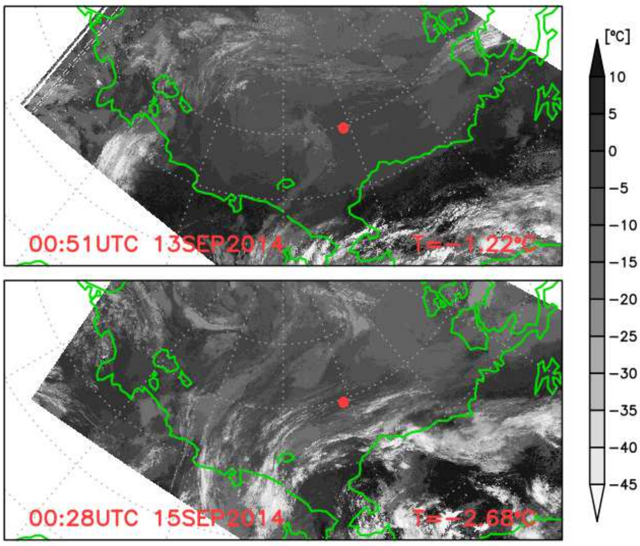

Fig. 1 Infrared satellite images (NOAA/AVHRR) received onboard *RV Mirai* on 13 and 15 September 2014. Red dot indicates location of fixed-point observations. Numeric value in the lower-right corner in each image is the infrared temperature at the fixed point.

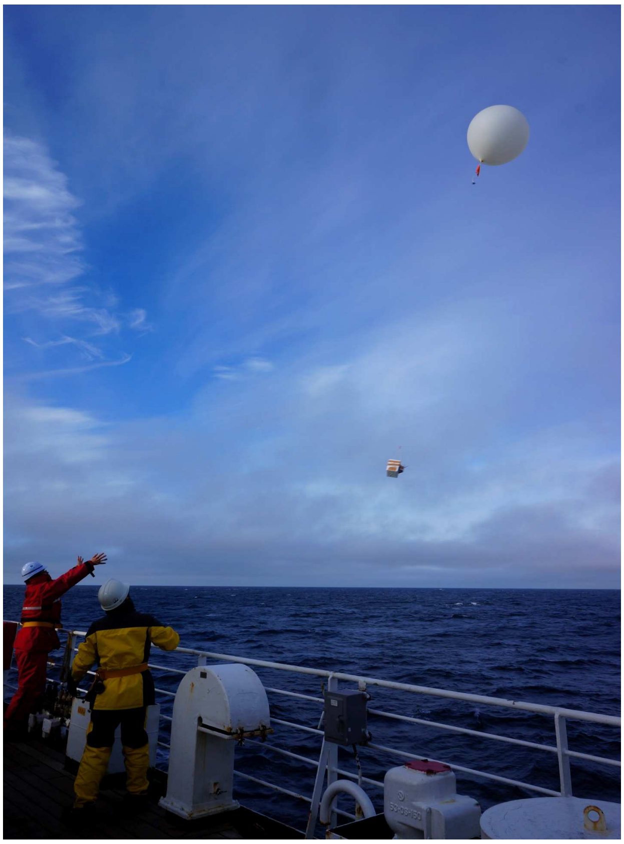

Fig. 2 Launching an ozonesonde from *RV Mirai* at 2200 UTC 14 September 2014.

and model outputs (e.g., Intrieri *et al.*, 2002; Inoue *et al.*, 2006; Schweiger *et al.*, 2008; Tjernström *et al.*, 2008; Sato *et al.*, 2012), the upper-tropospheric situation has not been evaluated fully. Because of Arctic amplification, moisture transport is enhanced, even in the upper troposphere, and vice versa (e.g., Maturilli and Kayser, 2016); thus, validation of the reproducibility at the upper troposphere using observation data is desirable.

In September 2014, as part of an Arctic research cruise undertaken by a Japanese research vessel in the Chukchi Sea, frequent fixed-point radiosonde observations and surface meteorological measurements were acquired. Using these data sets, this study investigated the reproducibility of the ERA-Interim reanalysis product with reference to the upper troposphere and related processes.

2. DATA

2.1 Radiosonde observations obtained during the *RV Mirai* Arctic cruise

In September 2014, two types of special radiosonde observations were performed during an Arctic cruise by *RV Mirai* under sea-ice-free conditions. One comprised regular 3-hourly (0000–2100 UTC) GPS radiosonde observations (RS92-SGPD, Vaisala) acquired above a fixed point in the Chukchi Sea (74.75°N, 162.00°W; red dot in Fig. 1) during 6–25 September 2014. After each observation, all data were sent to the World Meteorological Organization via the Japan Meteorological Agency and the global telecommunication system (GTS).

The other type of observation comprised ozonesonde observations (Fig. 2) acquired using Electrochemical Concentration Cell ozonesondes (6A, Science Pump Corp.), an Ozone Interface Kit (RSA921, Vaisala), and a GPS radiosonde (RS92-SGPD, Vaisala). Prior to launch, the ozone sensor was calibrated using an Electrochemical Concentration Cell Ozonesonde Ozonizer/Test Unit TSC-1 (Science Pump Corp.). Ozonesondes were launched every two days at 2200 UTC during 6–24 September 2014. The data were not sent to the GTS.

Ancillary data sets included surface meteorological observations including downward shortwave and longwave radiation, and satellite imagery acquired from the Advanced Very High Resolution Radiometer and received onboard the ship. For further information, the cruise report (Inoue, 2014) is available online (http://www.godac.jamstec.go.jp/catalog/data/doc_catalog/media/MR14-05_all.pdf).

2.2 ERA-Interim product

The ERA-Interim reanalysis product (Dee *et al.*, 2011) (hereafter, ERA-I) was validated using the sounding data acquired during the *RV Mirai* cruise. The horizontal and temporal resolutions of the product are 0.75° × 0.75° and six hours (0000, 0600, 1200, and 1800 UTC), respectively. The parameters used in this study were air temperature, relative humidity, ozone partial pressure, cloud cover, specific humidity, and surface downward radiation. Grid-point mean values, comprising the averages of the two grids (74.25°N, 162.00°W and 75.00°N, 162.00°W) closest to the fixed sampling point (Fig. 1) were used for comparison with the observed values.

3. RESULT

3.1 Validation of reanalysis

Figure 3 shows the vertical profiles of air temperature obtained from the ozonesonde soundings (2200 UTC) and ERA-I (0000 UTC). Because our 3-hourly regular radiosonde observations were assimilated into the ECMWF operational system (ECMWF, 2014), the vertical structure of air temperature is reproduced very well for each day, except for the minimum temperature near the tropopause. The tropopause height is deviated from 300 to 200 hPa because of the intrusion of upper potential vorticity (e.g., 11 September). In the lower troposphere, clear inversion layers can be observed on 7, 9, 11, 13, and 17 September, while in ERA-I, the inversion layer is reproduced on 7,13 and 17 September. In the lower stratosphere, the temperature is reproduced well.

The structure of relative humidity (Fig. 4) is very different to that of air temperature. The value in ERA-I is overestimated from 20% to 40%, particularly in the mid- and upper troposphere between 500 and 200 hPa although the relative humidity data by radiosondes were assimilated into the system. The vertical distribution of cloud cover in ERA-I indicates that upper-layer clouds are produced in all cases, except for 13 September. Based on the satellite image of 13 September, the infrared temperature at the ship position was established as −1.2°C, i.e., indicating sea surface temperature. Therefore, this day was a clear-sky case. Only in this case is the vertical structure of relative humidity reproduced relatively well. On the other dates, e.g., 15 September, it was cloudy and, in fact, the infrared temperature derived by the satellite was −2.7°C, which corresponded to the cloud-top temperature. However, the height at which the air temperature was equal to −2.7°C is near the surface (i.e., fog or stratus clouds), while in ERA-I, the cloud top is around 200 hPa because of the saturated condition at the upper troposphere. The vertical structure of specific humidity indicated that the difference was very small compared with relative humidity (not shown), suggesting there might be some problems in the parameterizations of relative humidity and cloud formation in ERA-I.

Ozone partial pressure is completely data-assimilation free in ERA-I. Therefore, it is worth comparing the ERA-I ozone profiles with our observations to assess the performance of ERA-I. Even though our ozone data were not transferred to the GTS, the vertical profiles are reproduced to some extent (Fig. 5). In the troposphere, the observed ozone partial pressure decreases slightly from the surface to the tropopause, while in the lower stratosphere, the value increases up to around 70 hPa. Here, we focus on upper-tropospheric ozone. The typical observed value between 300 and 200 hPa is approximately 2.0 mPa, which is the minimum value in each profile. However, most ERA-I profiles overestimate it by about 0.5 mPa near the tropopause. In other words, the ERA-I vertical gradient of ozone partial pressure is weaker than observed, suggesting that certain mixing processes must be active. One possibility comes from the overestimation of upper-layer cloud and the resultant cloud-top cooling which enhances the vertical mixing processes.

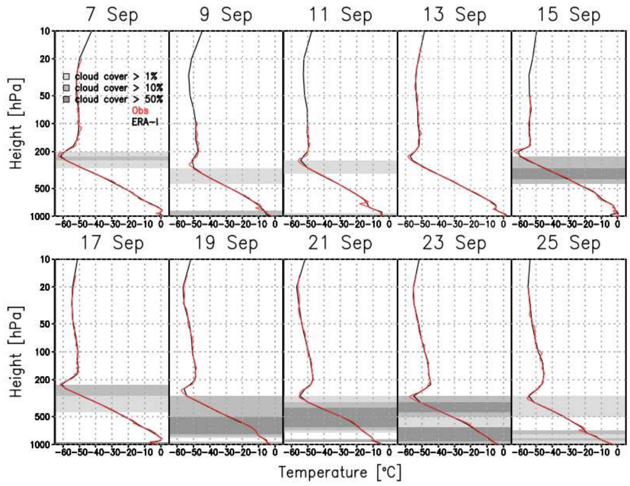

Fig. 3 Vertical profiles of air temperature based on ozonesonde data from *RV Mirai* (red line) and ERA-I values averaged over the two grids closest to the ship (black line) for each day. Gray shading indicates cloud cover in ERA-I (light gray: >1%, medium gray: >10%, dark gray: >50%).

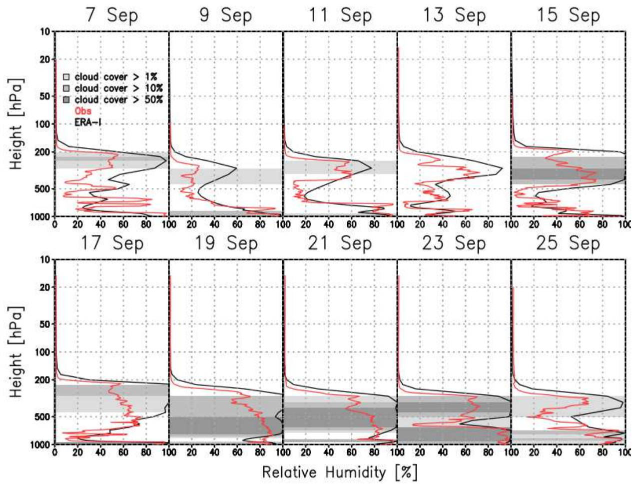

Fig. 4 As in Fig. 3 but for relative humidity.

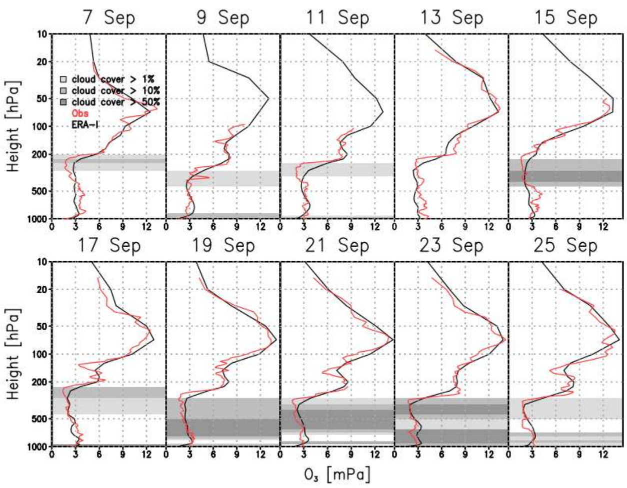

Fig. 5 As in Fig. 3 but for ozone partial pressure.

3.2 Parameterization of cloud and relative humidity in ERA-Interim

Generally, the performance of ERA-I is known as the best among the available reanalysis products, particularly in polar regions (e.g., Inoue *et al.*, 2011; Nicolas and Bromwich, 2011; Lindsay *et al.*, 2014). There have been many development points in ERA-I. One of the remarkable modifications is a new cloud parameterization based on Tompkins *et al.* (2007), which accounts for supersaturation with respect to ice in the cloud-free part of a grid box at temperatures <250 K (Dee *et al.*, 2011). Although they stated that this parameterization leads to substantial increase of relative humidity in the upper troposphere, methods to verify this parameterization are not available because of the bias of the relative humidity data obtained by radiosondes in the upper layers (e.g., Kawai et al., 2017). Nevertheless, the time–height cross sections of relative humidity, illustrated in Fig. 6, clearly show that ERA-I overestimates relative humidity throughout the entire period, particularly between the mid- and upper troposphere. As confirmed from the satellite imagery (Fig. 1; bottom), upper clouds were absent on 15 September, while ERA-I appears to have a thick cloud layer from 500 to 200 hPa (Fig. 7; top).

Following the implementation of a new moist boundary layer scheme in ERA-I (Köhler *et al.*, 2005; Köhler *et al.*, 2011), it was reported that marine cloud cover increased by 15%–25%, even over the Arctic Ocean (Dee *et al.*, 2011). This is partly consistent with our results shown in Fig. 7 (i.e., overestimation of cloud cover in the upper troposphere under cold conditions with temperatures <250 K). Time series of the downward shortwave and longwave radiation derived from the observations and ERA-I indicate that the overestimated upper-layer clouds sometimes affect the negative (positive) bias in shortwave (longwave) radiation (Fig. 7). For example, on 15 September (Figs. 1 and 2), the shortwave and longwave radiation was underestimated by more than 50 W m^{-2} and overestimated by more 20 W m^{-2}, respectively, in ERA-I. The converse situation was observed on 7 September mainly because of the lack of low-level clouds (see relative humidity in Fig. 6).

As reported by Dee *et al.* (2011), the entrainment process at the top of the boundary layer for the moist boundary layer is explicitly prescribed in terms of buoyancy flux with a surface buoyancy component (Troen and Mahrt, 1986; Holtslag, 1998) and a cloud-top radiative cooling component (Lock, 1998). Therefore, once upper-tropospheric clouds are formed, these buoyancy-driven mixing processes

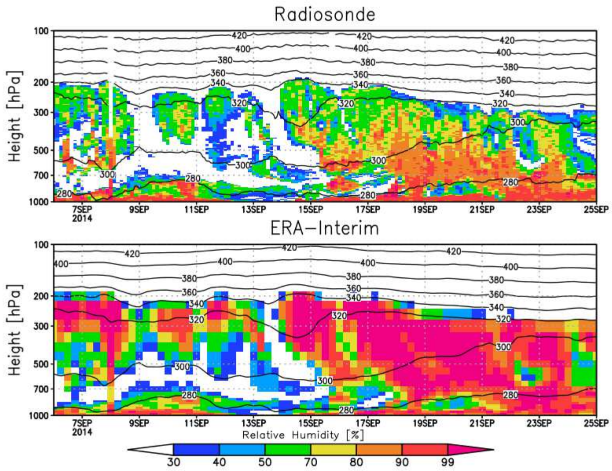

Fig. 6 Time–height cross sections of relative humidity (%: shading) and potential temperature (K: contours) based on observations (upper) and ERA-I

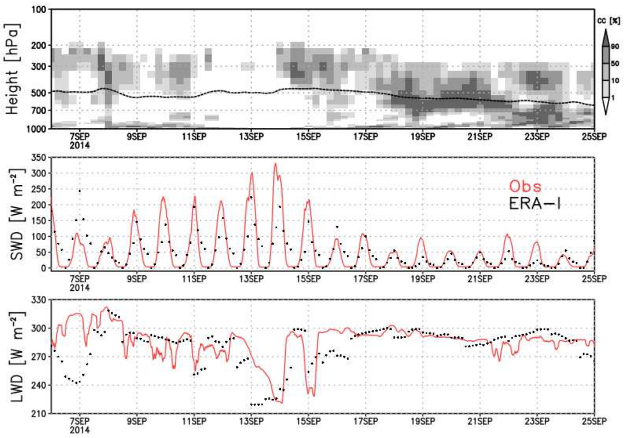

Fig. 7 Time–height cross sections of cloud cover in ERA-I (upper), and downward shortwave (middle) and longwave (lower) radiation based on observations (red line) and ERA-I (black dots). Black contour indicates air temperature of 250 K. Observed values are 3-h running means.

start. When the mass flux term is used to calculate the counter-gradient transport at the top of the overestimated clouds, additional biases would be expected in ERA-I. Here, we focus on the ozone partial pressure and relative humidity near the tropopause. If entrainment of a dry air mass with high ozone partial pressure were active from the lower stratosphere into the upper troposphere, because of evaporative and radiative cooling at the cloud top, the high-ozone air mass would be transported into the upper troposphere, whereas the moist air would be transported into the lower stratosphere. In fact, the ozone partial pressure in ERA-I is larger than observed, particularly for cloudy cases near the tropopause (Fig. 5). In addition, the relative humidity is overestimated in ERA-I above the tropopause, indicating that a small amount

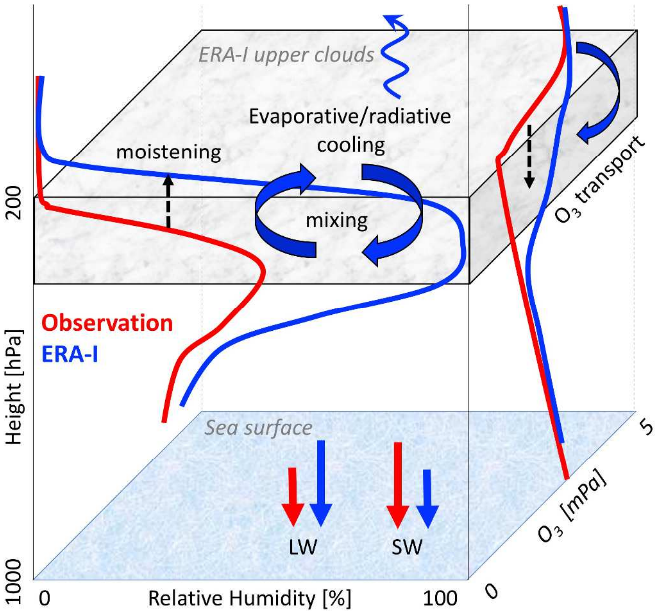

Fig. 8 Schematic of processes in ERA-I associated with overestimated upper-layer cloud (gray box). Red (blue) arrows and lines indicate the observed (ERA-I) situation of surface radiation and profiles of relative humidity and ozone partial pressure.

of moisture has been transported into the lower troposphere (Fig. 4).

In the real condition, based on our observations, relative humidity at the mid- and upper troposphere is relatively low; thus upper tropospheric clouds and evidences of mixing processes across the tropopause were not remarkable.

4. CONCLUSION

Using a tracer of ozone partial pressure, obtained by the ozonesondes launched from the *RV Mirai* over the Arctic Ocean, the ERA-Interim reanalysis product was evaluated by focusing on the mixing at the cloud top, moistening of the lower stratosphere, and surface radiation balance. A schematic summarizing the processes discussed in this study is illustrated in Fig. 8. Compared with the observations, excessive upper-tropospheric clouds were found in ERA-I because of conditions favorable for cloud formation. The ozone partial pressure near the tropopause was larger than observed, suggesting the downward transport of a high-ozone air mass across the tropopause via entrainment. Such a mixing process was also found in the relative humidity field with a moist bias in the lower stratosphere. These mixing processes would be caused by radiative/evaporative cooling at the cloud top. The overestimation of clouds in ERA-I also resulted in disagreement in the surface radiation balance in the case of absent low-level boundary layer clouds. Under ongoing Arctic amplification, the condition of humidity and the cloud condition at upper troposphere would be expected to become more important in understanding the radiation balance at the surface as well as at the top of the atmosphere. This study did not investigate the seasonal variability of the reproducibility of the ERA-Interim reanalysis product; however, a full years' special observations (e.g., Year of Polar Prediction: http://www.polarprediction.net/yopp-activities/; MOSAiC: http://www.mosaicobservatory.org/) would make such an evaluation possible in the near future.

ACKNOWLEDGMENTS

We thank the crew of the *R/V Mirai* and all the scientists who supported the observations. This work was supported by a Grant-in-Aid for Scientific Research (KAKENHI(A) 24241009) and the Arctic Challenge for Sustainability (ArCS) project. We thank James Buxton MSc from Edanz Group (www.edanzediting.com./ac) for editing a draft of this manuscript.

REFERENCES

Curry, J. A. and A. H. Lynch (2002): Comparing Arctic regional climate models. *EOS Trans. AGU*, **83**, 87.

Curry, J. A. and 26 others (2000): FIRE Arctic clouds experiment. *Bull. Amer. Meteorol. Soc.*, **81**, 5–29.

Dee, D. P. and 35 others (2011): The ERA-Interim reanalysis: configuration and performance of the data assimilation system. *Quart. J. Roy. Meteorol. Soc.*, **137**, 553–597.

ECMWF (2014): ECMWF global data monitoring report September 2014. *ECMWF*. Available at https://www.ecmwf.int/sites/default/files/mmr_201409.pdf.

Holtslag, A. A. M. (1998): Modelling of atmospheric boundary layers. In *Clear and cloudy boundary layers*. Holtslag, A. A. M. and P. Duynkerke, Eds., Royal Netherlands Academy of Arts and Sciences, 85–110.

Inoue, J. (2014): RV Mirai cruise report (MR14-05). *Japan Agency for Marine-Earth Science and Technology, Yokosuka, Japan*. Available at http://www.godac.jamstec.go.jp/catalog/data/doc_catalog/media/MR14-05_all.pdf.

Inoue, J., B. Kosović and J. A. Curry (2005): Evolution of a storm-driven cloudy boundary layer in the Arctic. *Bound.-Layer Meteorol.*, **117**, 213–230.

Inoue, J., J. Liu, J. O. Pinto and J. A. Curry (2006): Intercomparison of Arctic regional climate models: Modeling clouds and radiation for SHEBA in May 1998. *J. Clim.*, 19, 4167–4178.

Inoue, J., M. E. Hori, T. Enomoto and T. Kikuchi (2011): Intercomparison of surface heat transfer near the Arctic marginal ice zone for multiple reanalyses: A case study of September 2009. *SOLA*, **7**, 57–60.

Intrieri, J. M., M. D. Shupe, T. Uttal and B. J. McCarty (2002): An annual cycle of Arctic cloud characteristics observed by radar and lidar at SHEBA. *J. Geophys. Res.*, **107(C10)**, 8030.

Kawai, Y., M. Katsumata, K. Oshima, M. E. Hori and J. Inoue (2017): Comparison of Vaisala radiosondes RS41 and RS92 in the oceans ranging from the Arctic to tropics. *Atm. Meas. Tech.*, **10**, 2485–2498.

Köhler, M. (2005): Improved prediction of boundary layer clouds. *ECMWF Newsletter*, **104**, 18–22.

Köhler, M., M. Ahlgrimm and A. Beljaars (2011): Unified treatment of dry convective and stratocumulus-topped boundary layers in the ECMWF model. *Quart. J. Roy. Meteorol. Soc.*, **137**, 43–57.

Lindsay, R., W. Wensnahan, A. Schweiger and J. Zhang (2014): Evaluation of seven different atmospheric reanalysis products in the Arctic. *J. Clim.*, **27**, 2588–2606.

Liu, Y. and J. R. Key (2016): Assessment of Arctic cloud cover anomalies in atmospheric reanalysis products using satellite data. *J. Clim.*, **29**, 6065–6083.

Lock, A. P. (1998): The parameterization of entrainment in cloudy boundary layers. *Quart. J. Roy. Meteorol. Soc.*, **124**, 2729–2753.

Maturilli, M. and M. Kayser (2016): Arctic warming, moisture increase and circulation changes observed in the Ny-Ålesund homogenized radiosonde record. *Theor. Appl. Clim.*, doi:10.1007/s00704-016-1864-0.

Nicholls, S. and J. Leighton (1986): An observational study of the structure of stratiform cloud sheets: Part I. structure. *Quart. J. Roy. Meteorol. Soc.*, **112**, 431–460.

Nicolas, J. P. and D. H. Bromwich (2011): New reconstruction of Antarctic near-surface temperatures: Multidecadal trends and reliability of global reanalyses. *J. Clim.*, **27**, 8070–8093.

Sato, K., J. Inoue, Y.-M. Kodama and J. E. Overland (2012): Impact of Arctic sea-ice retreat on the recent change in cloud-base height during autumn. *Geophys. Res. Lett.*, **39**, L10503.

Schweiger, A. J., R. W. Lindsay, S. Vavrus, and J. A. Francis (2008): Relationships between Arctic sea ice and clouds during autumn. *J. Clim.*, **2**1, 4799–4810.

Tjernström, M., J. Sedlar, and M. D. Shupe (2008): How well do regional climate models reproduce radiation and clouds in the Arctic? An evaluation of ARCMIP simulations. *J. Appl. Meteorol. Climatol.*, **47**, 2405–2422.

Tompkins, A. M., K. Gierens and G. Rädel (2007): Ice supersaturation in the ECMWF integrated forecast system. *Quart. J. Roy. Meteorol. Soc.*, **133**, 53–63.

Troen, I. B. and L. Mahrt (1986): A simple model of the atmospheric boundary layer; Sensitivity to surface evaporation. *Bound.-Layer Meteorol.*, **37**, 129–148.

Uttal, T. and 27 others (2002): Surface heat budget of Arctic Ocean. *Bull. Amer. Meteorol. Soc.*, **83**, 255–275.

Summary in Japanese

和文要約

北極海上の気象観測データを用いたERA-Interim大気再解析プロダクトの対流圏上部の再現性

猪上淳[1]，佐藤和敏[2]，大島和裕[3]

[1]国立極地研究所, [2]タスマニア大学, [3]海洋研究開発機構

海洋地球研究船「みらい」を用いた北極海での約 3 週間にわたる定点観測を2014年9月に実施した．3時間毎のラジオゾンデ観測，2日毎のオゾンゾンデ観測，連続海上気象観測によるデータを用い，ERA-Interim 再解析プロダクトの再現性を評価した．気温・オゾン分圧・相対湿度の鉛直分布を比較したところ，気温の再現性が高いのに対し，相対湿度は対流圏中層から上部，および成層圏下部において 20%～40%過大評価，オゾン分圧は対流圏界面直下で 0.5mPa 過大評価していた．相対湿度の時間高度断面を比較すると，期間を通じて対流圏上部を中心に明瞭な湿潤バイアスが存在し，雲量も過大評価される傾向にあった．これは気温 250K よりも低温状態で活性化する ERA-Interim 内の雲生成のパラメタリゼーションが主要因であると示唆される．雲頂部の放射・蒸発冷却による混合過程は，成層圏下部からの高オゾン気塊のエントレインメント（下方輸送），および対流圏上部の湿潤気塊の上方輸送を促すと考えられ，観測結果ともとも整合的であった．上層雲のバイアスは海面放射バランスにも影響を与え，特に下層雲を伴わない場合に顕著に現れた．

Copyright ©2018 The Okhotsk Sea & Polar Oceans Research Association. All rights reserved.

Okhotsk Sea and Polar Oceans Research 2 (2018) 13-18
© Okhotsk Sea and Polar Oceans Research Association
https://doi.org/10.57287/ospor.2.13

Article

Development of a new algorithm to estimate Arctic sea-ice thickness based on Advanced Microwave Scanning Radiometer 2 data

Kazutaka TATEYAMA[1], Jun INOUE[2], Seita HOSHINO[3], Shota SASAKI[1] and Yasuhiro TANAKA[1]

[1]*Kitami Institute of Technology, Kitami, Hokkaido, Japan*
[2]*Arctic Environment Research Center, National Institute of Polar Research, Tachikawa, Japan*
[3]*Graduate School of Engineering, Kitami Institute of Technology, Kitami, Hokkaido, Japan*

Abstract

Data from the Advanced Microwave Scanning Radiometer 2 (AMSR2) are used to evaluate the Arctic sea-ice thickness (SIT). The polarization ratio at 36 GHz (PR_{36}) and the gradient ratio between 6 and 36 GHz ($GR_{06\text{-}36}$), which contain the signals for the first-year ice and multi-year ice thicknesses, respectively, are used to estimate the draft of the sea-ice. The developed equation for the SIT is validated using SIT results derived from ice mass balance (IMB) buoys and the results are compared with the SIT data obtained from Cryosat-2 (CS2). For SIT calculations performed for the period from March to September, a seasonal bias correction was applied to the SIT that was derived from the AMSR2 algorithm based on the skin temperature, which was determined from an atmospheric reanalysis. This correction reduced the SIT error effectively; however, large errors that occur during the melting and refreezing season still remain because the existence of melt ponds and their refreezing affect the microwave radiation strongly. Improvement of the regional biases outside the validation area will be also necessary.

Key words: sea-ice thickness, passive microwave radiometer, AMSR2, Cryosat-2, ice mass balance buoy

(Received October 4, 2017; Revised manuscript accepted January 18, 2018)

1. INTRODUCTION

The annual to decadal variability of the Arctic sea-ice volume is highly relevant for evaluation of the Arctic fresh water budget and global climate change. The extent of the Arctic sea-ice has been monitored continuously using satellite-borne passive microwave radiometers such as the Scanning Multichannel Microwave Radiometer (SMMR) and the Special Sensor Microwave Imager (SSM/I) since the late 1970s (Comiso *et al*., 2008). However, acquiring observations of changes in the ice thickness has been challenging, and several approaches have been used to date. For example, the thin sea-ice thickness (SIT) with no snow has been provided by satellite-borne visible and infrared radiometers (Yu and Rothrock, 1996; Drucker *et al*., 2003) and passive and active microwave sensors (Kwok *et al.*, 1999, Giles *et al*., 2008; Tamura *et al*., 2008). Recently, a thick SIT algorithm was developed using altimeter data from both ICESat (e.g., Kwok *et al*., 2007) and Cryosat-2 (e.g., Laxon *et al*., 2013). However, these altimeters provide the ice thickness distributions monthly and weekly, but not daily.

A daily sea-ice draft estimation algorithm was developed for the Advanced Microwave Scanning Radiometer-EOS (AMSR-E), which was onboard the Earth Observing Satellite Aqua of the U.S. National Aeronautics and Space Administration (NASA); Aqua was launched in 2002, but stopped rotating in 2011. The algorithm was devised on the basis of in situ sea-ice draft data that were derived from upward looking sonar (ULS) devices mounted on mooring buoys in the Beaufort Gyre. These buoys have been located in the southern Canada basin since 2002 (Krishfield *et al.*, 2014). While the algorithm is corrected for seasonal errors using statistical methods, major underestimations occur in spring and summer.

In this study, the AMSR-E thickness algorithm was applied to data from a new microwave radiometer: the Advanced Microwave Scanning Radiometer 2 (AMSR2), located onboard the Earth observation satellite Global Change Observation Mission-Water (GCOM-W) of the Japan Aerospace Exploration Agency (JAXA), which was launched in 2012. Here, we evaluate the SIT values derived from the AMSR2 data and compare them with the in situ thicknesses derived from drifting buoys and other satellite sensors.

2. DATA AND METHOD

We used the brightness temperature (*TB*), which is observed twice a day by AMSR2 and provided at 10 km resolution in a polar stereographic projection from the JAXA, to calculate the sea-ice draft using the estimation algorithm that was developed for AMSR-E data (Krishfield *et al.*, 2014).

We evaluated the validity of the sea-ice draft thickness that was estimated from the AMSR2 data by comparing our results with the thicknesses measured using the satellite-borne altimeter that is mounted on Cryosat-2 (CS2) and in situ measurement results from ice mass balance (IMB) buoys.

2.1 Sea-ice draft algorithm

Cavalieri *et al.* (1984) defined the following sea-ice parameters: the gradient ratio (*GR*; Eq. 1) and the polarization ratio (*PR*; Eq. 2). These parameters are used to calculate ice concentrations for first-year (FY) ice and multi-year (MY) ice, respectively, as follows:

$$GR = \frac{TB_{\mathrm{V}} - TB'_{\mathrm{V}}}{TB_{\mathrm{V}} + TB'_{\mathrm{V}}} \tag{1}$$

$$PR = \frac{TB_{\mathrm{V}} - TB_{\mathrm{H}}}{TB_{\mathrm{V}} + TB_{\mathrm{H}}}. \tag{2}$$

Krishfield *et al.* (2014) suggested that the *PR* at 36 GHz (PR_{36}) and the *GR* in the range between 6 GHz and 36 GHz (GR_{06-36}) could be used to estimate the sea-ice drafts of FY ice and MY ice, respectively. They defined the sea-ice draft $D_{\mathrm{AMSR-E}}$ estimation formulae in the two equations below. When GR_{06-36} is greater than −0.035, the sea-ice type is regarded as FY ice, and Eq. 3 is used to estimate $D_{\mathrm{AMSR-E}}$:

$$\begin{aligned} &\text{FY ice } D_{\mathrm{AMSR-E}}\ [\mathrm{m}] \\ &= 2.34\exp\left(\frac{PR_{36} - 0.0019}{0.0283}\right) + 0.085 \end{aligned} \tag{3}$$

Conversely, when GR_{06-36} is less than −0.035, Eq. 4 is used to estimate $D_{\mathrm{AMSR-E}}$:

$$\begin{aligned} &\text{MY ice } D_{\mathrm{AMSR-E}}\ [\mathrm{m}] \\ &= 0.244\exp(-20.785 GR_{06-36}) + 0.162 \end{aligned} \tag{4}$$

These formulae are based on in situ ice draft measurements from the ULS devices mounted on four mooring buoys from 2002 to 2011 in the Beaufort Sea; their locations are shown as stars in Fig. 1. In this context, the ice draft is the ice thickness below the waterline, while the ice freeboard is the ice thickness above the waterline. The SIT is generally defined as the total freeboard plus the ice draft.

A seasonal bias in the sea-ice draft derived from mooring buoys and AMSR-E data has been found (Krishfield *et al.*, 2014). This seasonal fluctuation is most likely to be caused by changes in the ice surface properties, such as melting during spring and summer, or snow during autumn and winter.

In this study, we applied the AMSR-E ice draft algorithm to AMSR2 data and validated the algorithm's effectiveness based on CS2 and IMB thicknesses.

2.2 Cryostat-2 thickness data

Monthly mean SIT data observed by the Synthetic Interferometric Radar Altimeter (SIRAL) onboard the CS2 satellite, which was launched by the European Space Agency in April 2010, were compared with the FY ice and MY ice draft thickness values estimated from the AMSR2 data. SIRAL is a microwave radar with a central frequency of 13.6 GHz that uses the $\mathrm{K_U}$ band to measure the sea-ice freeboard. The SIT can then be calculated from the freeboard value using the hydrostatic equilibrium (Laxon *et al.*, 2013).

We used the CS2 sea-ice freeboard, ice thickness, and snow depth data set projected on the EASE2.0 grid, which was provided by the Alfred Wegener Institute (Ricker *et al.*, 2014). This data set is available for the Arctic winter and spring seasons only, i.e., from October to May.

In this study, the monthly mean CS2 SIT and the monthly mean $D_{\mathrm{AMSR-E}}$ were compared at the locations shown in Fig. 1. Data sampling points were set at 85, 80, and 75°N and 0, 30, 60, 120, 135, 150, 165, 180°E and °W over the ice-covered area.

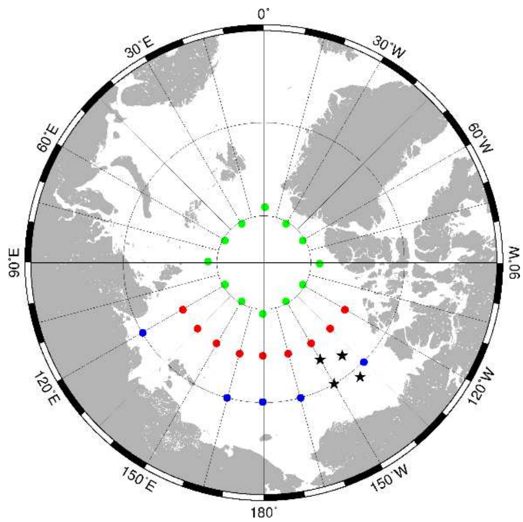

Fig. 1 Data sampling points for sea-ice draft and thickness located along 85°N (green), 80°N (red), and 75°N (blue). The stars and dots correspond to the daily sea-ice draft measurements based on ULS and AMSR2 data, respectively, during the period from 2002–2011 and the monthly mean CS2 derived SIT and AMSR2 sea-ice draft values from 2012 to 2013.

2.3 Ice mass balance buoy thickness data

The IMB buoys were deployed in the Arctic in 1993 and have provided datasets since 1993, which are available from the U.S. Army Engineer Research and Development Center's Cold Regions Research and

Engineering Laboratory. The IMB dataset contains hourly snow depth, ice thickness, sea-ice temperature profile, air temperature, barometric pressure, and ice drift data (see e.g., Richter-Menge *et al.*, 2006; Polashenski *et al*., 2011).

The daily $D_{\mathrm{AMSR-E}}$ value was compared with the daily mean in situ SIT and the air and water temperatures, air pressure and snow depth measured by five IMB buoys during the period from 2012–2013. Fig. 2 shows the thickness distributions along the IMB tracks around the North Pole and the Canada basin.

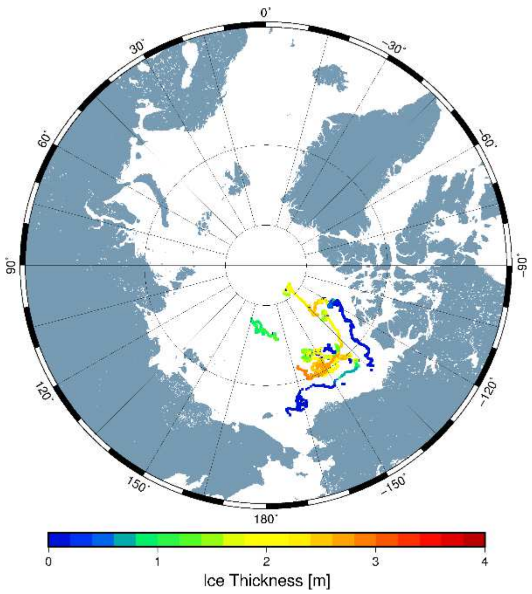

Fig. 2 SIT distributions along IMB tracks from 2012–2013.

3. RESULTS AND DISCUSSION

3.1 Comparison between CS2 thickness and AMSR2 draft

Figure 3 shows the results of our comparison between the monthly mean CS2 thicknesses and the AMSR2-derived draft using Krishfield's algorithm from October to May for 2012–2013. Figure 3a shows clear differences between the AMSR2 draft and the CS2 thickness along both the longitudinal and latitudinal ranges. There is an obvious regional bias that leads to a large underestimation in the western Arctic region related to the existence of MY ice and a relative overestimation in the eastern Arctic region related to Russian river discharges, which cause thicker sea-ice because of lower surface salinity over the ice surface.

Figure 3b shows seasonal variations in the AMSR2 draft and CS2 thickness along longitudes of 120°W, 180°E, and 120°E. Each longitude shows a seasonal bias, in which the AMSR2 data underestimate the draft towards the beginning of spring and show high scattering in autumn. Along 120°W, the AMSR draft tends to be underestimated throughout the year. The same underestimation appeared on 85 and 80°N but not on 75°N along 120°E. This seasonal bias probably reflects the high sensitivity of the microwave sensor to changes in sea-ice surface characteristics, particularly during the melting season from early spring to summer, and during the early stages of snow freezing on the melted surface. To identify the causes and improve the seasonal bias in the SIT, we compared in situ sea-ice surface changes.

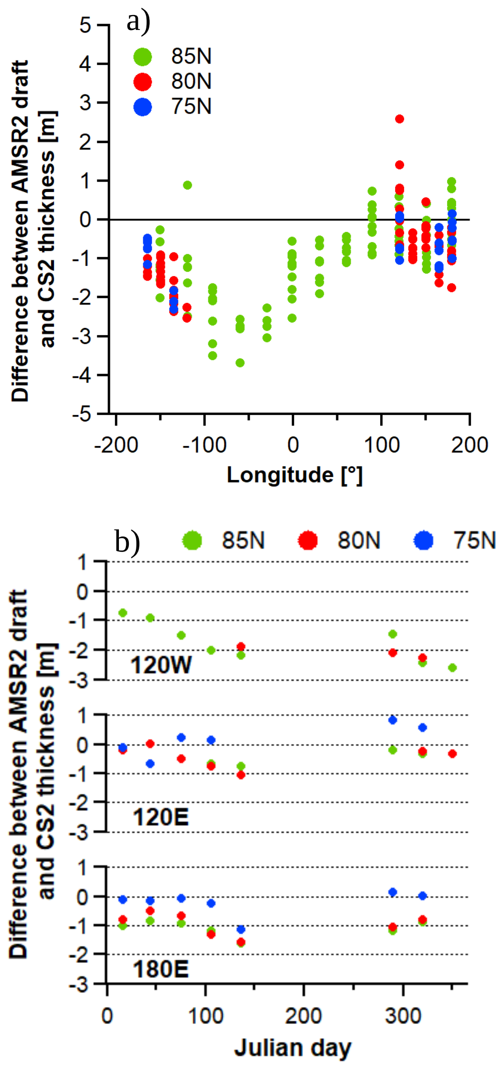

Fig. 3 Comparisons between monthly mean CS2 thickness and AMSR2 draft. a) Longitudinal cross-sections are along 85°N (green dots), 80°N (red dots), and 75°N (blue dots). Positive and negative longitudes mean East and West, respectively. b) Seasonal cross-sections along 120°W, 120°E, and180°E longitudes.

3.2 Comparison between IMB thickness, air temperature and AMSR2 draft

We analyzed the relationship between the AMSR2 draft and IMB SIT values to obtain a conversion formula from the AMSR2 draft D_{AMSR2} to the AMSR2 SIT H_{AMSR2}. The relationship between the IMB SIT

H_{IMB} and D_{AMSR2} values from September to February and their regression line are shown in Fig. 4. A conversion formula based on Fig. 4 is given as Eq. 5.

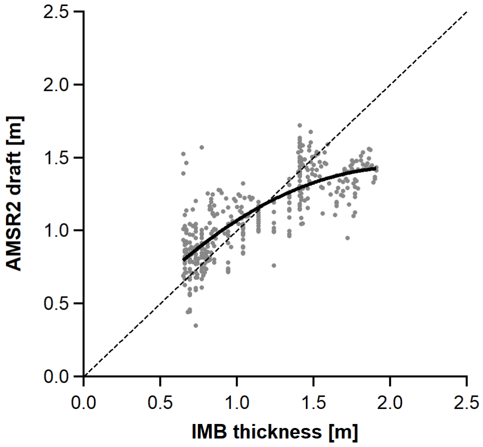

Fig. 4 Scatter diagram showing daily IMB SIT values for the five buoys shown in Fig. 2 versus the sea-ice draft estimated from AMSR2 data using Eq. 3 or 4.

Because the underestimation of the AMSR2 draft values increased over the period from winter to spring (Fig. 3d–f)), we investigated the differences in SIT values between H_{AMSR2} and H_{IMB} as a function of near-surface air temperature for all seasons (Fig. 5). The air temperature was closely correlated with the thickness difference between the values derived from AMSR2 and the IMB buoys. This indicates that there could be further improvements in the performance of the AMSR2 draft algorithm if a near-surface variable is used as a correction factor in Eq. 5.

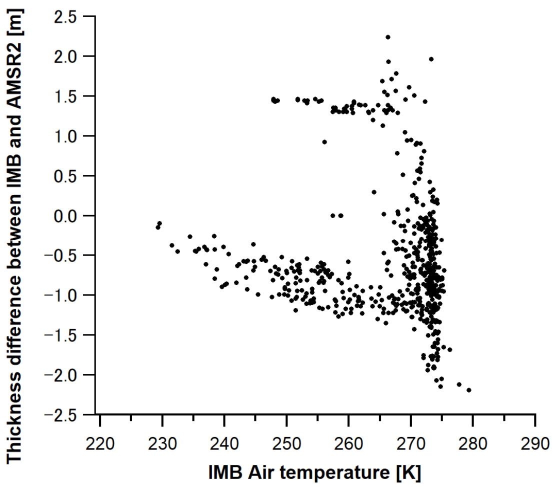

Fig. 5 Differences in thickness between IMB and AMSR2 methods, reflecting the effects of air temperature for both the autumn and winter data sets.

$$H_{\mathrm{AMSR2}}\ [\mathrm{m}] = 0.0477 + 0.821 D_{\mathrm{AMSR2}} + 0.134 {D_{\mathrm{AMSR2}}}^2 \quad (5)$$

However, because the air temperature data are obtained from drifting buoys over the Arctic Ocean, they are not generally assimilated into the reanalysis products, making them less useful for SIT estimation because of the large associated uncertainty. Instead, the skin temperature of the ice surface, which is determined using the surface heat budget, particularly the radiation balance from spring to autumn, is likely to be a more suitable parameter.

Figure 6a shows the relationship between the in situ air temperature derived from the IMB buoys and the skin temperature provided by the European Centre for Medium-Range Weather Forecasts (ECMWF) for 2012–2013. The skin temperature has a high correlation coefficient ($R = 0.98$ from March to May, with an annual value of $R = 0.95$).

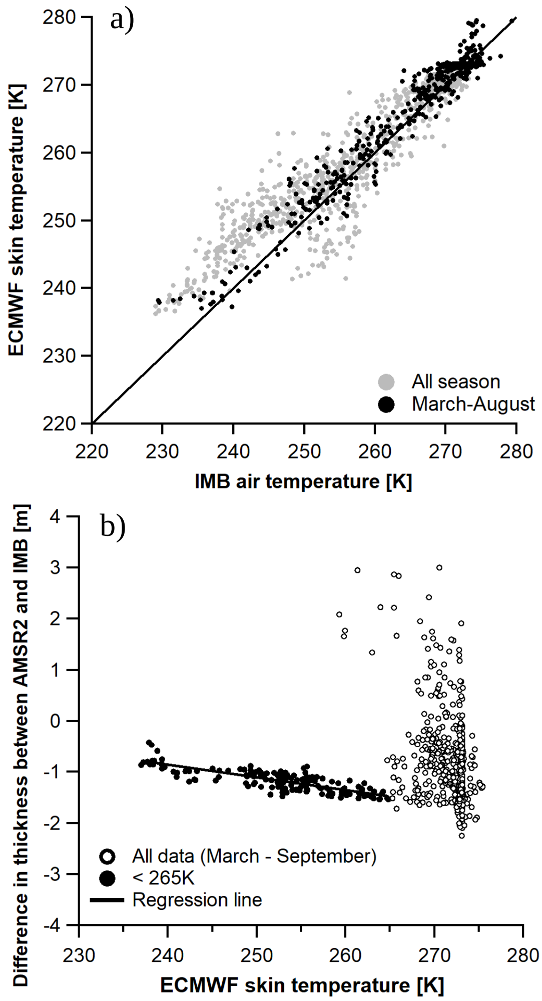

Fig. 6 a) Relationship between skin temperature provided by the ECMWF and in situ air temperature derived from the IMB, and b) the difference in SIT between the AMSR2 and IMB derivations during 2012–2013.

Figure 6b shows seasonal changes in skin temperature lower than 265 K (black dots) and the difference in thickness between H_{AMSR2} and H_{IMB} from March to September (gray dots). There is a systematic large difference in thickness as a function of skin temperature when it is lower than 265 K.

By focusing on temperatures of less than 265 K, the thickness deviation between H_{AMSR2} and H_{IMB} can be characterized as a linear function of the ECMWF skin temperature with a high correlation coefficient (R = –0.81). In this case, H_{AMSR2} can be corrected based on the skin temperature (T_{skin}) when it is lower than 265 K from March to September using Eq. 6.

$$H'_{\mathrm{AMSR2}}\ [\mathrm{m}] = H_{\mathrm{AMSR2}} - (5.07 - 0.0247T_{skin}) \qquad (6)$$

We confirmed that Eq. 6 is valid for the period from March to September. While Krishfield *et al*. (2014) attempted to estimate the SIT over the Beaufort Sea using ULS observations, their equation still requires correction as a function of the Julian day to improve its empirical seasonal bias. The *TB* is a function of both temperature and emissivity (Cavalieri *et al.*, 1984). When the emissivity is constant, a change in skin temperature contributes to the *TB* change. This correction would be dependent on the latitude at which the in situ observations were made. In contrast, Eqs. 5 and 6 were generated from a larger area of the Arctic Ocean, which makes our algorithm more robust.

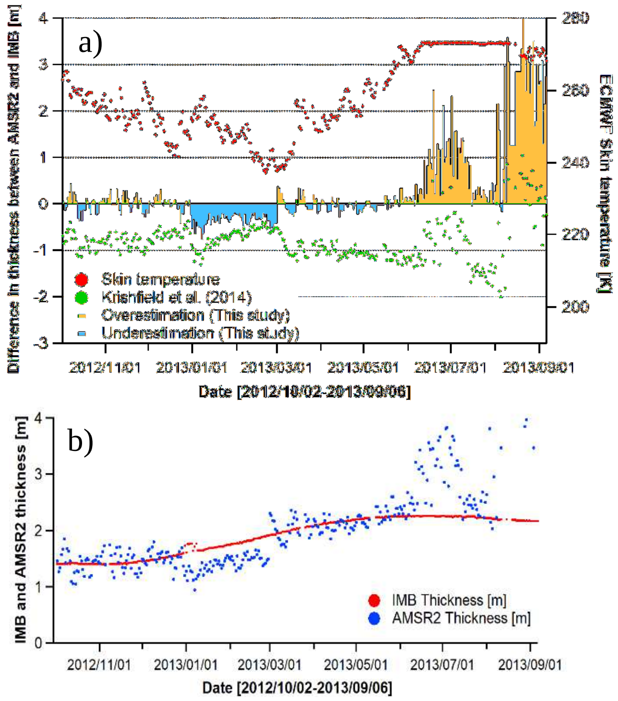

Fig. 7 Examples of skin temperature, differences in thicknesses between IMB and AMSR2 data and corrected AMSR2 draft values based on skin temperature in Eq. 6.

Finally, we investigated the validity of the H'_{AMSR2} values by comparing H'_{AMSR2} with H_{IMB}. Figure 7a shows an example of the relationships among skin temperature (red dots), and the SIT differences when determined using Krishfield's algorithm (green dots) and using the algorithm proposed here (blue and orange bars). The underestimation that was described previously for our algorithm increases as the skin temperature rises from March to June. Additionally, the large overestimates from June to September are likely to correspond to refreezing of melt ponds. The passive microwave radiometer is very sensitive to phase changes on the ice surface. This suggests that we could improve H_{AMSR2} estimates using the skin temperature during spring and autumn. The blue and orange bars in Fig. 7 show improvements related to skin temperature correction. Clearly, the thickness difference was minimized from March to June. Figure 7b shows better agreement between the IMB and AMSR2 results during the spring and summer seasons, suggesting that this modified algorithm provides more reliable SIT data for the spring and early summer periods.

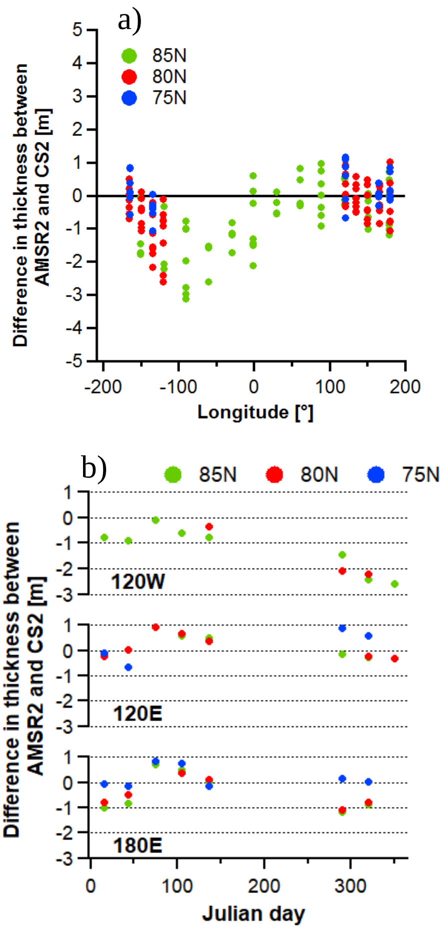

Fig. 8 Comparisons between monthly mean CS2 thickness and modified AMSR2 thickness along with the data of Fig. 3. a) Longitudinal cross-sections and b) seasonal cross-sections.

Comparisons between the monthly mean CS2 thickness and the modified AMSR2 thickness are shown in Fig.8. While a large underestimate remains in the western Arctic, the overall underestimated offset was improved using Eq. 5. The seasonal bias was also removed during the period from March to May.

Figure 9 shows an example of SITs estimated from AMSR2 data using a) Krishfield's algorithm and b) our improved SIT algorithm for 1 April 2013. Our improved SIT values are more than 2 m thick, which is approximately 1 m thicker than the values obtained using Krishfield's algorithm. This thicker ice area indicates thickness of more than 5 m in the north of Canadian Arctic Archipelago, which resembles the monthly CS2 SIT values in appearance.

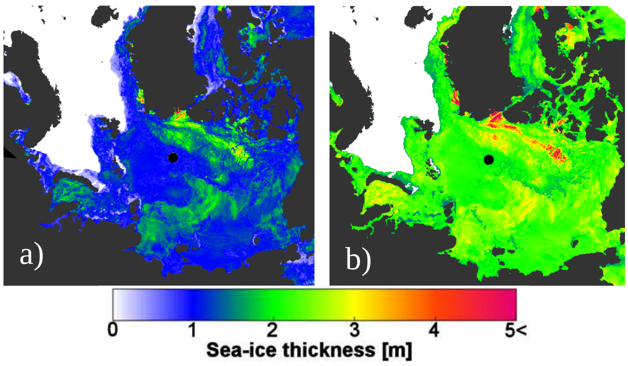

Fig. 9 Examples of AMSR2 SIT on April 1, 2013: a) with Julian day correction; b) with skin temperature correction.

4. CONCLUSIONS

A SIT algorithm for AMSR2 data was newly developed for the Arctic sea-ice in this study. The ice draft was estimated from AMSR2 data using an algorithm that was adapted from one designed for the AMSR-E data (Krishfield *et al.*, 2014). Ice draft values were converted to thicknesses by comparing them with the in situ thicknesses observed by IMB buoys from 2012 to 2013. The thickness differences among the CS2-, IMB- and AMSR2-based methods show seasonal variations because the microwave frequency is sensitive to phase changes on the ice surface. This seasonal bias was successfully minimized from March to June using the skin temperatures derived from the ECMWF. There also is a regional bias to the SIT estimates, in which SIT underestimation over the western Arctic is related to existence of MY ice. The algorithm was improved and validated within the Arctic Ocean via comparisons with CS2 and IMB data, as shown in Figs. 1 and 2. Therefore, there are overestimates of the SIT outside the validation area (e.g., Bering Sea, Sea of Okhotsk). Improvement of these regional biases is an issue for future work.

ACKNOWLEDGEMENTS

This study was supported by the Japanese Green Network of Excellence Program (GRENE), the Arctic Climate Changes Research Project, the Arctic Challenge for Sustainability Project (ArCS), and the Japan Society for the Promotion of Science (JSPS) Grants-in-Aid for Scientific Research (A) (grant no. JP26249133) and Scientific Research (C) (grant no. JP26340013). We are grateful to Dr. Richard Krishfield and Dr. Takuya Nakanowatari for their collaboration and advice. We also thank Dr. Trudi Semeniuk and David MacDonald, MSc, from Edanz Group for editing drafts of this manuscript.

REFERENCES

Cavalieri, D.J., P. Gloersen and W. J. Campbell (1984): Determination of sea ice parameters with the NIMBUS 7 SMMR, *J. Geophys. Res.*, **89**(D4), 5355–5369.

Comiso, J. C., and F. Nishio (2008): Trends in the sea ice cover using enhanced and compatible AMSR-E, SSM/I, and SMMR data, *J. Geophys. Res.*, **113**, C02S07, doi:10.1029/2007JC004257.

Drucker, R., S. Martin, and R. Moritz (2003): Observation of ice thickness and frazil ice in the St. Lawrence Island polynya from satellite imagery, upward looking sonar, and salinity/temperature moorings, *J. Geophys. Res.*, **108**(C5), 3149, doi:10.1029/2001JC001213.

Giles, K. A., S. W. Laxon, and A. L. Ridout (2008): Circumpolar thinning of Arctic sea ice following the 2007 record ice extent minimum, *Geophys. Res. Lett.*, **35**, L22502, doi:10.1029/2008GL035710.

Krishfield, R. A., A. Proshutinsky, K. Tateyama, W. J. Williams, E. C. Carmack, F. A. McLaughlin and M.-L. Timmermans (2014): Deterioration of perennial sea ice in the Beaufort Gyre from 2003 to 2012 and its impact on the oceanic freshwater cycle, *J. Geophys. Res.*, **119**(2), 1271–1305.

Kwok, R., Cunningham, G., Zwally, H., and Yi, D. (2007): Ice, Cloud, and land Elevation Satellite (ICESat) over Arctic sea ice: retrieval of freeboard, *J. Geophys. Res.*, **112**, C12013, doi:10.1029/2006JC003978.

Kwok, R., G. F. Cunningham, N. LaBell-Hamer, B. Holt, and D. A. Rothrock (1999): Sea ice thickness from high-resolution SAR imagery, *Eos Trans. AGU*, **80**, 495–497.

Laxon, S. W. and 14 co-authors (2013): CryoSat-2 estimates of Arctic sea ice thickness and volume, *Geophys. Res. Lett.*, **40**, 732–737, doi:10.1002/grl.50193.

Polashenski, C., D. K. Perovich, J. A. Richter-Menge, B. Elder (2011): Seasonal Ice Mass-Balance Buoys: Adapting tools to the changing Arctic. *Ann. Glaciol.*, **52** (57), 18-26.

Richter-Menge, J. A., et al. (2006): Ice mass balance buoys: A tool for measuring and attributing changes in the thickness of the Arctic sea ice cover, *Ann. Glaciol.*, **44**, 205 – 210.

Ricker, R., Hendricks, S., Helm, V., Skourup, H., and Davidson, M. (2014): Sensitivity of CryoSat-2 Arctic sea-ice freeboard and thickness on radar-waveform interpretation, *The Cryosphere*, **8**, 1607–1622, doi:10.5194/tc-8-1607-2014.

Tamura, T., K. I. Ohshima, and S. Nihashi (2008): Mapping of sea-ice production for Antarctic coastal polynyas. *Geophys. Res. Lett*. **35**, L07606.

Yu, Y. and D. A. Rothrock (1996): Thin ice thickness from satellite thermal imagery, *J. Geophys.Res.*, **101**, 25,753-25,766.

Copyright ©2018 The Okhotsk Sea & Polar Oceans Research Association. All rights reserved.

Submission Information for OSPOR

Reviewing processes of OSPOR

1) When manuscripts have been received by the Editor-in-Chief, an acknowledgement of receipt will be sent to the author(s) by e-mail. The Editor-in-Chief chooses an editor to handle the manuscript review.
2) The submitted manuscript will be subjected to screening review for its scope, novelty, completeness, English level, and conformation to the OSPOR policy. A manuscript not passing the screening review will immediately be returned to the authors.
3) The editor in charge will select expert reviewers to evaluate the manuscript.
4) As to results of review, if the editor decides that the paper needs revision by the author(s), the manuscript will be returned to the author(s) for revision.
5) Manuscripts returned to author(s) for revision should be resubmitted promptly. If the revision cannot be finished within a month, the manuscript will be regarded as having been withdrawn.
6) The Editor-in-Chief will finally decide whether to accept the manuscript for publication.

Paper Submission

Submission Guideline

All manuscripts should be submitted in digital format (PDF or WORD) with the OSPOR submission sheets (PDF or WORD, offered from OSPOR) by email to the OSPOR Editorial Board

OSPOR Editorial Board

Polar Oceans Research Association (OSPORA)

Address: Kaiyo Koryukan, 1 Kaiyo Koen, Mombetsu, Hokkaido 094-0031 Japan
E-mail: momsys@o-tower.co.jp
Phone : +81-158-26-2810 (Japan 0158-26-2810)
Fax: +81-158-26-2812 (Japan 0158-26-2812)

Publication Charge

Authors of their institutions are requested to pay the publication charge according to the following rate when paper is accepted.
5,000 Yen / (paper)

Copyright

Copyright for an article submitted to OSPOR is transferred to OSPORA when the article is published in OSPOR in any form.

Preparation of manuscripts

The manuscript should be formatted in the form of OSPOR template offered from the OSPORA office, which satisfies the following requirements. The maximum page in printing style is 6 pages.

1) Text
   a) The manuscript should be in the international size A4 in camera-ready style according to the form of OSPOR template.
   b) The first page should include: the title, the author(s) name(s) and their affiliations. If possible, a Japanese translation of the title and the name(s) of the author(s) should be provided in the end of manuscript. If they are not, the translation will be undertaken by the OSPOR editorial board.
   c) An abstract not exceeding 250 words must be provided.
   d) Up to five keywords that describe the content for indexing purposes must be provided.

2) References

a) A list of cited references should be arranged alphabetically. Journal abbreviations are better to use, but when the abbreviation is not known, the full title of the journal should be used in the list.

In the case of many authors, the author name can be written in short as below.

Kawamura, K., F. Parennin and 16 others (2007): Northern hemisphere forcing of climatic cycles in Antarctica over the past 360,000 years. *Nature*, **448**, 912-916.

b) References in the text will include the name(s) of the author(s), followed by the year of publication in parentheses, *e.g.* (Clarke, 2003), (Li and Sturm, 2002), (Harrison *et al*., 2001).

3) Units

Numerical units should conform to the International System (SI).

Units should be in the form as kg m^{-3} not as kg/m^3.

4) Tables

A title and a short explanation should be located on the top of table.

They should be referred to in the text.

5) Figures

a) All Figures (illustrations and photographs) should be numbered consecutively.

b) All Figures should be of good quality and referred to in the text.

c) Figure captions should be located on the bottom of the Figures.

6) More information

For more information about manuscript instruction, please ask to OSPORA office or see OSPORA home page in http://www.o-tower.co.jp/okhsympo/top-index.html.

Okhotsk Sea and Polar Oceans Research, Vol. 2 (2018, February)

Published by the Okhotsk Sea and Polar Oceans Research Association (OSPORA),
Mombetsu City, Hokkaido, Japan

Executive Committee of OSPORA:

Chairman: Shuhei Takahashi (Okhotsk Sea Ice Museum of Hokkaido, Director)

Secretariat: Eriko Uematsu

Address: Kaiyo Koryukan, 1 Kaiyo Koen, Mombetsu, Hokkaido 094-0031 Japan

E-mail: momsys@o-tower.co.jp

Phone : +81-158-26-2810 (Japan 0158-26-2810)

Fax: +81-158-26-2812 (Japan 0158-26-2812)

http://www.o-tower.co.jp/okhsympo/top-index.html

Okhotsk Sea and Polar Oceans Research Vol. 2 2018

Okhotsk Sea and Polar Oceans Research

Published by the Okhotsk Sea and Polar Oceans Research Association (OSPORA)
Mombetsu City, Hokkaido, Japan